



OPEN

Carbon fibres as potential bone implants with controlled doxorubicin release

Dorota Chudoba^{1,2}✉, Katarzyna Łudzik^{3,2} & Monika Jażdżewska^{1,2}

This work presents the structural characterisation of carbon fibres obtained from the carbonization of flax tow at 400°C (CFs400°C) and 1000°C (CFs1000°C) and the thermodynamic and kinetic studies of adsorption of Doxorubicin (Dox) on the fibres. The characteristic of carbon fibres and their drug adsorption and removal mechanism were investigated and compared with that of natural flax tow. All fibres were fully characterized by scanning electron microscopy (SEM), Fourier transforms infrared spectroscopy (FT-IR), thermogravimetric analysis (TGA), specific surface area analysis and Boehm titration. The results demonstrated the highest adsorption properties of CFs400°C at 323 K ($q_{\max} = 275 \text{ mg g}^{-1}$). The kinetic data followed the pseudo-second-order kinetic model more closely, whereas the Dubinin–Radushkevich model suitably described isotherms for all fibres. Calculated parameters revealed that the adsorption process of Dox ions is spontaneous and mainly followed by physisorption and a pore-filling mechanism. The removal efficiency for carbon fibres is low due to the effect of pore-blocking and hydrophobic hydration. However, presented fibres can be treated with a base for further chemical surface modification, increasing the adsorption capacity and controlling the release tendency.

For decades, carbon materials have been regarded as the most promising and useful products because of their important properties such as thermal stability, mechanical resistance, environment-friendliness, chemical inertness, bio and hemocompatibility^{1–9}. The development of nanotechnology, fabrication and modification of carbon materials caused an enormous increase of scientific and industrial attention due to the new and broader spectrum of their potential applications that can improve the quality of life. A large share of works is those devoted to the use of carbon nanomaterials to biomedicine as nanocontainers^{9–16}. The features of carbon nanomaterials such as large surface volume, porosity and functional surface meant that many types of drugs and antibodies could be chemically conjugated to their surface. Thus, carbon nanomaterial systems can deliver drugs and improve the stability of the drugs and prevent their uncontrolled uptake and removal. An additional advantage of carbon nanomaterials is that covalently modified carbon materials do not accumulate in organs but are prone to be excreted through urine¹⁷.

One promising candidate from a huge and various groups of carbon-based materials is produced from pyrolysis of organic precursor-like polyacrylonitrile or pitch in an inert atmosphere—carbon fibres, alternatively abbreviated as CFs^{18,19}. These materials with a micro graphite crystal structure and low density, similar to bond density ($1.6\text{--}2.2 \text{ g/cm}^3$) exhibit unusual mechanical properties such as high specific strength or flexibility^{19,20}. The superior properties in conjunction with electrical conductivity, high radiolucency, biocompatibility, inert nature and shape, that mimics the crystalline hydroxyapatite structures of natural bone, make the carbon fibres potential constituents of medical devices for structural fixation of skeleton fragments^{3,20–26}. In addition, carbon fibres exhibit specific bioactivities in relation to the location in the living body. R. Petersen or K. Elias emphasize the ability of CFs to osseointegrate with live bone and reliability to stimulate tissue to grow and heal by removing respiratory stress products^{20,24}. R. Price confirms dimension dependent cell adhesion on carbon filaments, which is crucial for dental or orthopaedic materials^{26,27}. Although the surface of carbon filaments does not affect cell adsorption, it plays a crucial role in determining their end-use performance as a reinforcement for composite materials and effects on immunological cells response and adsorption ability²⁸. Thus, controlled modification or functionalization of the surface of CFs can enhance properties and use those materials as a scaffold for tissues with simultaneously releasing drugs supporting regeneration or treatment.

¹Faculty of Physics, Adam Mickiewicz University, Poznan 61-614, Poland. ²Frank Laboratory of Neutron Physics, Joint Institute for Nuclear Research, Dubna 141980, Russia. ³Department of Physical Chemistry, University of Lodz, 90-236 Lodz, Poland. ✉email: dmn@amu.edu.pl

It has been documented that the nature of precursor and selection of carbonization parameters affect structure and mechanical properties of carbon fibres^{29,30}. The type and degree of activation determine its physical and chemical properties.

In this study, we characterized the structure of three types of fibres: flax tow—pristine fibres pFs, fibres after carbonization at 400°C (CFs400°C), fibres after carbonization at 1000°C (CFs1000°C) and investigated from the kinetic and thermodynamic point of view process of adsorption and release of doxorubicin hydrochloride (Dox). A better understanding of the interaction mechanism of Dox with carbon fibres as well as kinetic and thermodynamic of adsorption and release of the drug will provide opportunity to realize the most effective strategy for their surface modification and in consequence exhibits the opportunity to use the material as a bone implants with controlled Dox release.

Experimental

Materials. Carbon fibres (CFs) were prepared from a natural precursor—flax tow (pFs) at Warsaw University. The pristine materials are in the form of carbonaceous fibres with a diameter below 100 µm. The chemical composition of flax is similar to other bio-resources. The flax is a mixture of polymerized units of glucose (lignin, pectin and hemicelluloses). The surface modification included thermal annealing at two different temperatures: 400°C (CFs400°C) and 1000°C (CFs1000°C). The thermal treatment causes carbonization and changes the surface chemistry. The process was carried out in a tube furnace equipped with a gas matrix (inert atmosphere Ar to eliminate possible oxidation processes) with a heating rate of 5 °C min⁻¹. Afterwards, the furnace was cooled down naturally. Doxorubicin hydrochloride (purity ≥ 98%, Sigma Aldrich) -Dox, was used without further purification. All solutions were prepared in Milli-Q (The Millipore ultrapure water Co., Ltd., Millipore, Burlington, MA, USA) ultrapure water.

Samples characterisation. Surface chemical features were studied by FT-IR spectroscopy (Thermo Fisher Nicolet iS5) and EDX spectrometry (Zeiss Merlin equipped with EDX spectrometer). FT-IR measurements were carried out in a transmission mode with a spectral resolution of 4 cm⁻¹. A little amount of the studied sample (ca. 1 mg) was mixed with 300 mg KBr and pressed in a hydraulic press. The content of surface acidic groups was determined from Boehm titration by using Metrohm automatic titrator Titrando 808.

Scanning electron microscopy was used to determine morphological features (Zeiss Merlin equipped with EDX spectrometer). Before measurements, the studied samples were covered by a thin conductive layer.

The porous structure of the samples was evaluated by physical adsorption of N₂ at 77 K in a Micromeritics ASAP 2020 apparatus. By using the Brunauer-Emmitt-Teller equation the specific surface area was determined. Pore volumes were estimated at a relative pressure of 0.94 p/p⁰, assuming full surface saturation with nitrogen. Pore size distributions were evaluated from desorption branches of nitrogen isotherms using the Barret-Joyner-Halenda (BJH) model.

Thermogravimetric analyzer TA Instruments TA Q50 was used for the characterization of pure CFs and CFs with adsorbed doxorubicin (the heating rate of 5 deg min⁻¹ and nitrogen atmosphere).

Dox adsorption efficiency and drug release processes were investigated spectroscopically by means of UV-Vis: Shimadzu 2401 spectrophotometer as described previously³¹.

Equilibrium adsorption studies. The isotherms of Dox on investigated carriers were determined as follows. A known mass of the material was added to the solution containing various initial concentrations of doxorubicin in PBS buffer (2–700 mg L⁻¹). The as-obtained mixtures were shaken for 24 h. Next, the decrease of Dox concentration was determined spectrophotometrically using a standard curve method³². The data obtained in equilibrium studies were used to calculate the equilibrium Dox adsorptive quantity by using the following mass balance:

$$q_e = \frac{(C_0 - C_e)V}{m} \quad (1)$$

where: q_e is the amount of Dox adsorbed at equilibrium (mg g⁻¹), V is the volume of solution treated (L), C_0 is the initial concentration of Dox (mg L⁻¹), C_e is the equilibrium Dox concentration (mg L⁻¹) and m is the mass of the adsorbent (g).

The adsorption studies were carried out at three constant temperatures: 298.15 K 310.15 K and 323.15 K. All experiments were conducted in triplicate and the mean values have been reported. The equilibrium data were fitted with the Langmuir, Freundlich, Dubinin-Radushkevich (D-R) equilibrium adsorption isotherm models^{33–38}.

Adsorption kinetics studies. The adsorption kinetic curve of doxorubicin onto pristine and surface modified materials were determined similarly to the determination of adsorption isotherms. The adsorption kinetics was determined for the initial concentration of doxorubicin of 100 mg mL⁻¹. The mixtures were shaken for the specified time interval (5–15 min). The maximum contact time was 120 min. Finally, the decrease of Dox concentration was determined spectrophotometrically using a standard curve method³¹. The amount of drug adsorbed at time t , q_t (mg g⁻¹), was calculated by the Eq. (2):

$$q_t = \frac{(C_0 - C_t)V}{m} \quad (2)$$

where C_t (mg L⁻¹) is the concentration of Dox at any time t .

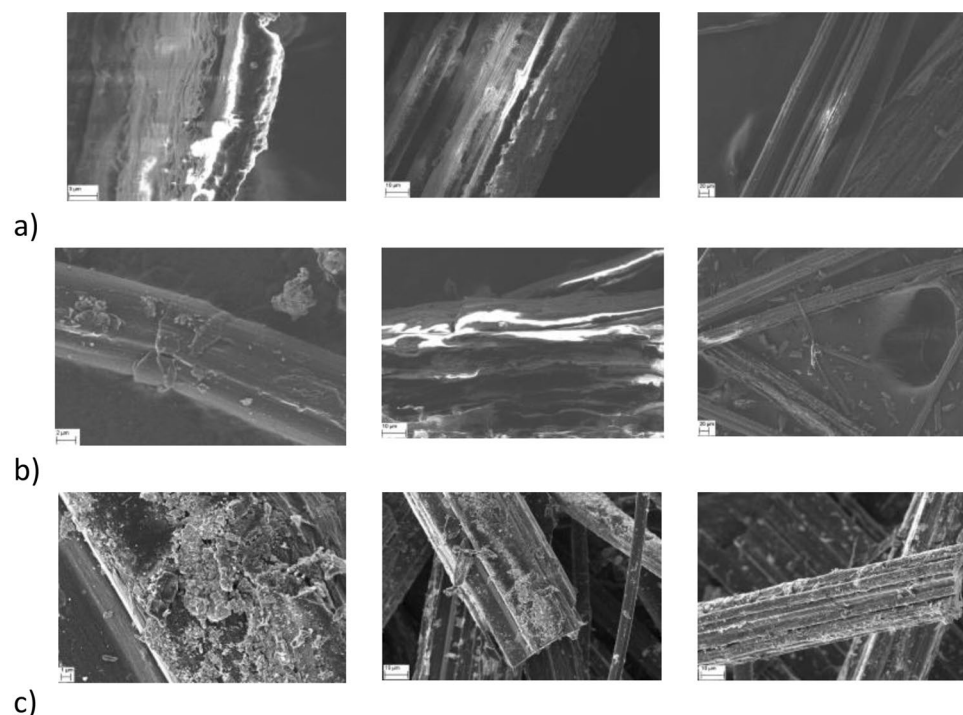


Figure 1. SEM images of: pure flax tow (in scale from left: 3 μ m, 10 μ m, 20 μ m) (a); carbonaceous flax fibres obtained after having been heated at 400 °C (in scale from left: 2 μ m, 10 μ m, 20 μ m) (b) and of carbonaceous flax fibres obtained after having been heated at 1000°C (in scale from left: 1 μ m, 10 μ m, 10 μ m) (c).

Studies on release of doxorubicin. The acetic buffer was chosen as the liquid medium for the studies on the doxorubicin release. The buffer was prepared by dissolving 0.1 mol (8.2 g) of sodium acetate in 1 L of 0.1 M acetic acid solution. The resulting pH was measured and it was equivalent to 4.95–5.05. The release of Dox from all pristine and surface modified materials was as follows: ca. 10 mg of the materials with adsorbed Dox was suspended in the specified volume of the medium and shaken for 24 h. Next, the solid material was separated by filtration or centrifugation. The concentration of Dox was determined spectrophotometrically using a standard curve method.

The kinetics of release of doxorubicin in acetic buffers was studied by preparation of several mixtures. In each one ca. 10 mg of the material with adsorbed Dox was placed in the acetic buffer. The volume of this medium was 50 mL. The mixtures were shaken for specified time intervals. Again, the concentration of released doxorubicin was determined spectrophotometrically. The kinetic results of Dox release process were presented as a function of % Dox released in time t Eq. (3):

$$\text{release \% Dox} = \frac{C_t}{C_0} 100\% \quad (3)$$

where C_t —concentration of drug released in t time, C_0 —maximum drug concentration obtained during the release process.

Results

Fibres characterisation. The morphological analysis of used filaments was carried to elucidate the adsorption and release mechanisms of doxorubicin on/from the fibres. The representative microscopy images of three types of investigated fibres: flax tow, fibres after carbonization at 400°C and at 1000°C were presented in Fig. 1a–c respectively. It is well visible that all the samples exhibit “fibrous” morphology. The rough surface is noticeable in case of CFs1000°C. The diameter of obtained fibres varies between 8 to 80 μ m. The shape of the fibres after carbonisation is oblate Fig. 1c (on the right).

The shape of the TGA curve for flax tow is typical and reflects the volatilization of water and adsorbed substances (100–250°C) and then char formation. TGA curves of investigated fibres determined under non-oxidizing atmosphere are presented in the supplementary materials—Figure S1. In the case, CFs400°C mass, the loose mass observed on the TGA curve can be attributed to the decomposition and thermal degradation of functional groups. In addition, the wide range of temperatures of loose mass suggests a different type of labile oxygen-containing groups on the CFs400°C surface. Similarly, the smooth shape of the TGA curve in case CFs1000°C confirms the marginal amount of functional groups on the fibre surface and the high thermal stability of the sample. In order to investigate the types of acidic groups, Boehm titration was applied. The result is presented in the supplementary materials—Table S1.

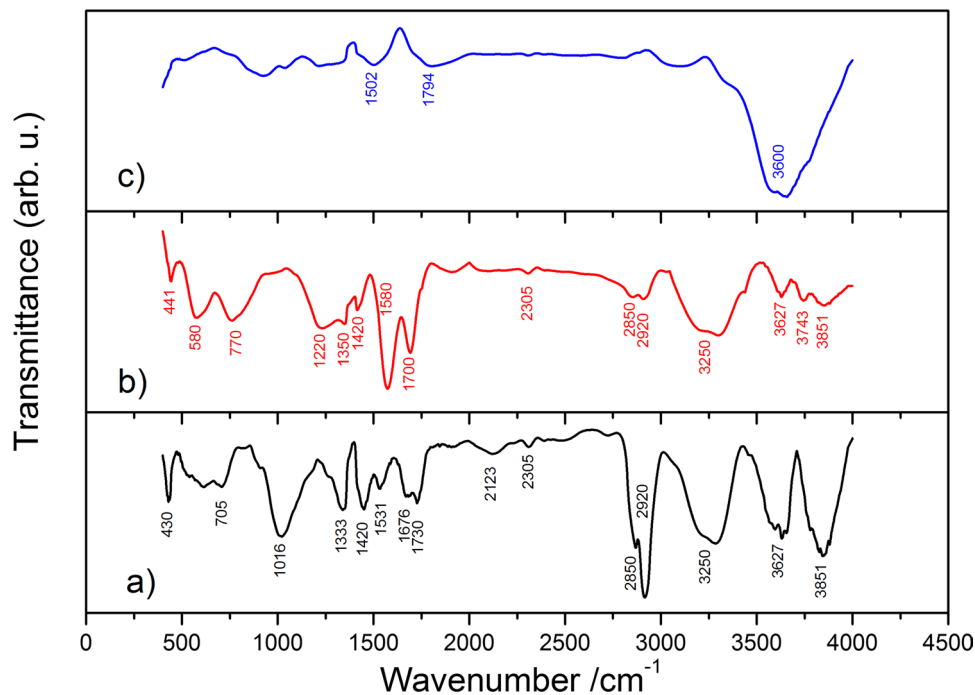


Figure 2. Fourier transform infrared spectroscopy (FT-IR) spectra of: (a) pFs, (b) CFs400°C (c) CFs1000°C.

Types of functional groups were also determined based on Fourier transform infrared spectroscopy (FT-IR) Fig. 2.

As is well seen in Fig. 2c, for CFs1000°C sample the broad peak at 3600 cm^{-1} reflects the stretching vibration of $-\text{OH}$ groups. In case CFs400°C—Fig. 2b, peaks from 3600–3800 cm^{-1} can be attributed to stretching vibration of not associated OH groups. The peak at 3250 cm^{-1} is assigned to stretching vibration of able to create hydrogen bonds $-\text{OH}$ groups. The peaks at 2850 and 2920 cm^{-1} indicate stretching vibration of C-H groups. Regarding the peaks at 1700, 1580, 1400, 1420, 1350, 1220 cm^{-1} it can be said that indicates the existence of asymmetric and symmetric stretching vibration of C=O groups, stretching vibration of aromatic C=C groups and stretching C-O groups. Obtained spectra of CF400°C confirms the existence of phenolic and lactonic groups that was concluded from Bohem titration. Small peaks from range 580–770 cm^{-1} are due to bending vibrations of $-\text{OH}$ groups^{39,40}.

Characterisation of the surface area of fibres was carried out by using nitrogen adsorption/desorption. The main textural parameters of investigated fibres were collected in the supplementary materials Table S2. It shows that pFs and CFs400°C practically do not contain micropores. What is more, the volume of narrow mesopores (2–10 nm) does not exceed 0.009 $\text{cm}^3 \text{g}^{-1}$, which is also marginal. As a result, the specific surface area for both samples is low. This is an expected finding because pF and CFs400°C have a rather non-porous surface presented on SEM images. Carbonization at 1000°C causes an increase of porosity (mainly micropores 0.031 $\text{cm}^3 \text{g}^{-1}$) and develops the specific surface area Fig. 1c.

Doxorubicin adsorption and release. The characterisation of a carrier with Dox was carried out by using SEM, TGA, FT-IR techniques and nitrogen adsorption tests. SEM results presented in Fig. 3 confirm that doxorubicin molecules have been grafted on the surface of carbon fibres. It is worth noticing that the adsorption of the drug is more efficient in case of pFs and CFs400°C than CFs1000°C.

From the TGA measurements (presented in the supplementary materials Figure S2) it can be stated that fibres with Dox yield more weight loss than pure fibres, which is attributed to the degradation of organic components of the vulnerable under such a high thermal condition drug.

The textural characteristic after adsorption and pore distribution before and after the drug adsorption were analysed to understand the mechanism of doxorubicin adsorption and its relationship with surface structure. The results were presented in the supplementary materials Table S3 and Figure S3.

Adsorption of Dox exhibits pore-size dependent tendency. The change in the pore size suggests that molecules of Dox do not occupy micropores lower than 4 nm. It is worth noticing that materials with very low porosity ($S_{\text{BET}} < 10 \text{ m}^2 \text{g}^{-1}$) can exhibit artefacts on the curves.

Adsorption isotherm and thermodynamic studies. In order to explore the process of Dox adsorption on fibres in more depth three equilibrium adsorption isotherm models: Freundlich, Langmuir and Dubinin–Radushkevich were applied to the adsorption equilibrium data presented in Fig. 4. Carbon fibres obtained at 1000°C have much more unsatisfactory adsorption performance in comparison to the pristine fibres and CFs400°C sample. Therefore, further studies of adsorption were not carried out on that sample.

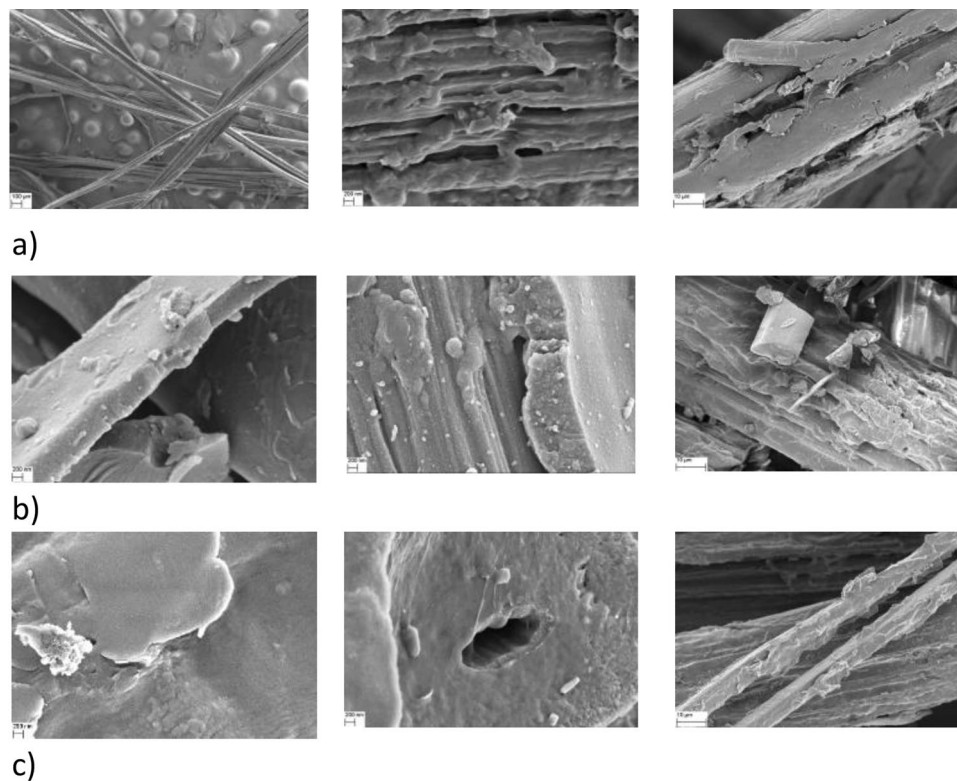


Figure 3. SEM images of: pure flax fibres with adsorbed molecules of Dox (in scale from left: 100µm, 200nm, 10µm) (a); carbonaceous flax fibres obtaining after having been heated at 400 °C with adsorbed molecules of Dox (in scale from left: 200nm, 200nm, 10µm) (b); carbonaceous flax fibres obtaining after having been heated at 1000°C with adsorbed molecules of Dox (in scale from left: 200nm, 200nm, 10µm) (c).

The earliest known relationship describing adsorption on heterogenous surfaces with active sites with different energy is Freundlich isotherm^{37,41}:

$$q_e = K_F C_e^{1/n} \quad (4)$$

where: q_e is the amount of Dox adsorbed per unit weight of adsorbent at equilibrium (mg g^{-1}), C_e the equilibrium concentration of Dox in the bulk solution (mg L^{-1}), K_F is adsorption capacity $\text{mg}^{1-1/n} \text{L}^{1/n} \text{g}^{-1}$ and $1/n$ is heterogeneity factor.

Langmuir isotherm assumes that adsorption takes place at a finite number of identical and energetically equivalent sites and the adsorbed layer is one molecule in thickness of monolayer adsorption³⁶. The Langmuir equation can be described by Eq. (5):

$$q_e = \frac{q_m K_L C_e}{1 + K_L C_e} \quad (5)$$

where: q_e is the amount of drug adsorbed per unit weight of adsorbent at equilibrium (mg g^{-1}), C_e —the equilibrium concentration of Dox in the bulk solution (mg L^{-1}), q_m the maximum adsorption capacity (mg g^{-1}), and K_L is the constant related to the free energy of adsorption (L mg^{-1}).

Adsorption mechanism on heterogeneous surfaces that follows a pore-filling mechanism can be described by temperature-dependent semi-empirical equation proposed by Dubinin Radushkevich³⁸:

$$q_e = q_m \exp \left[-\beta \left(RT \ln \left(1 + \frac{1}{C_e} \right) \right)^2 \right] \quad (6)$$

where: q_e is the maximal amount of drug adsorbed per unit weight of adsorbent at equilibrium (mg g^{-1}), C_e the equilibrium concentration of Dox in the bulk solution (mg L^{-1}), q_m (mg g^{-1}) is a constant related to adsorption capacity, R —gas constant, T is absolute temperature, β ($\text{g}^2 \text{kJ}^{-2}$) is a constant related to the mean free energy of adsorption $-E$ (kJ g^{-1}):

$$E = \frac{1}{\sqrt{2\beta}} \quad (7)$$

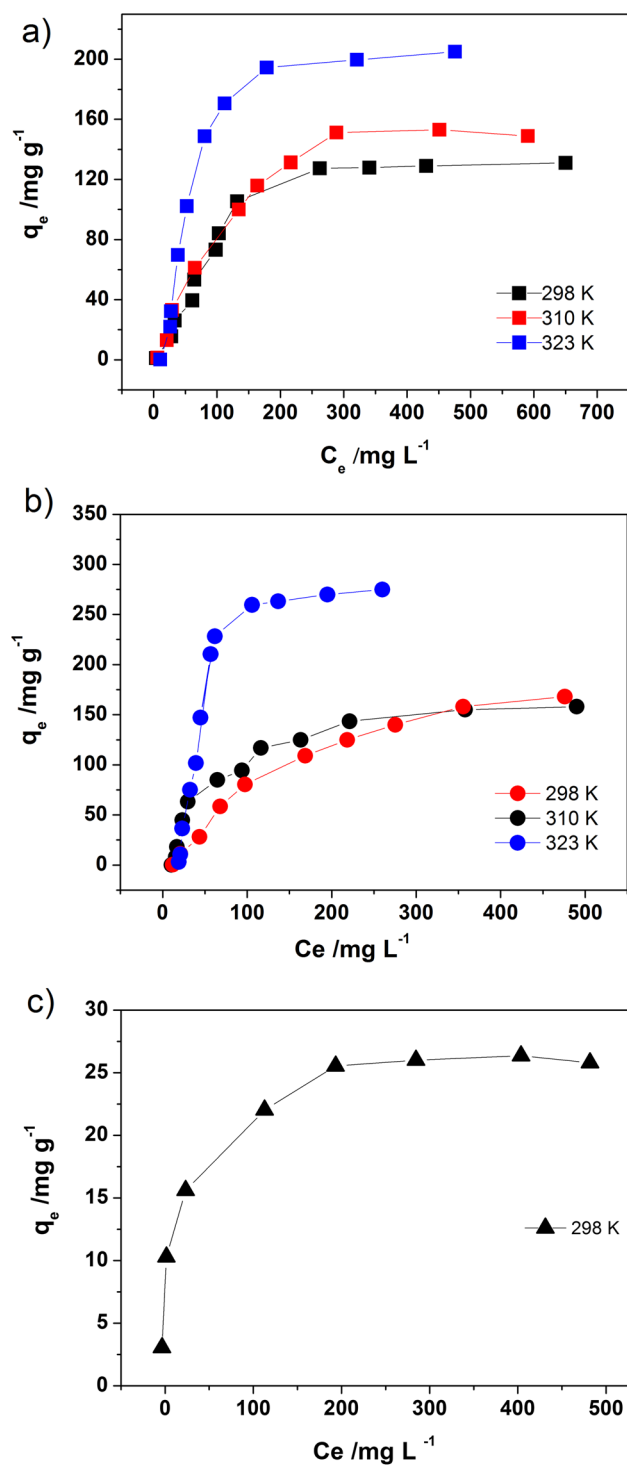


Figure 4. Adsorption isotherms of Dox on (a) pFs; (b) CFs400°C; (c) CFs1000°C.

The magnitude of E is the main criterion for determining the type of adsorption mechanism. The value of the free energy $< 8 \text{ kJ mol}^{-1}$ suggests physical adsorption^{42,43}, the value of E in the range 8–16 kJ/mol , indicates the adsorption process follows ion exchange⁴⁴. Values of E higher than 20 kJ/mol indicates chemisorption^{45,46}. The constant parameters of the two-parameter isotherm models were calculated by nonlinear regression analysis using Origin 9 and presented in Table 1.

Table 1 shows that the Dubinin-Radushkevich isotherm model can generate a satisfactory fit to the experimental data for pFs, CFs400°C and CFs1000°C within all investigated temperature ranges. Moreover, obtained from D-R model values of q_m are comparable with the experimental q_{max} (Table S4 supplementary materials) and correspond to the adsorption isotherm plateau (Fig. 4).

Fiber	The value of parameters for isotherm model		
	Freundlich	Langmuir	Dubinin–Radushkevich
pFs	T = 298 K		
	$K_F = 9.126$	$q_m = 172.8$	$q_m = 131.4$
	$n = 2.280$	$K_L = 0.0076$	$r^2 = 0.979$
	$r^2 = 0.847$	$r^2 = 0.944$	$E = 5.9$
	T = 310 K		
	$K_F = 9.826$	$q_m = 198.7$	$q_m = 148.0$
	$n = 2.208$	$K_L = 0.0077$	$r^2 = 0.984$
	$r^2 = 0.881$	$r^2 = 0.973$	$E = 5.8$
	T = 323 K		
	$K_F = 15.220$	$q_m = 269.5$	$q_m = 200.8$
	$n = 2.231$	$K_L = 0.0104$	$r^2 = 0.994$
	$r^2 = 0.768$	$r^2 = 0.901$	$E = 7.9$
CFs400°C	T = 298 K		
	$K_F = 4.178$	$q_m = 200.2$	$q_m = 133.7$
	$n = 1.626$	$K_L = 0.0102$	$r^2 = 0.973$
	$r^2 = 0.949$	$r^2 = 0.980$	$E = 14.0$
	T = 310 K		
	$K_F = 11.039$	$q_m = 266.3$	$q_m = 172.4$
	$n = 2.210$	$K_L = 0.0039$	$r^2 = 0.969$
	$r^2 = 0.870$	$r^2 = 0.959$	$E = 5.36$
	T = 323 K		
	$K_F = 17.214$	$q_m = 417.6$	$q_m = 290.1$
	$n = 1.892$	$K_L = 0.0108$	$r^2 = 0.982$
	$r^2 = 0.665$	$r^2 = 0.775$	$E = 10.5$
CFs1000°C	T = 298 K		
	$K_F = 9.878$	$q_m = 27.2$	$q_m = 26.8$
	$n = 6.037$	$K_L = 0.0550$	$r^2 = 0.950$
	$r^2 = 0.962$	$r^2 = 0.958$	$\chi^2 = 3.885$
	$\chi^2 = 2.974$	$\chi^2 = 0.748$	$E = 2.3$

Table 1. Freundlich, Langmuir and Dubinin–Radushkevich isotherm parameters obtained by nonlinear fitting for the three types of fibres: pFs, CFs400°C and CFs1000°C for: 298, 310, 323 K. $q_m/\text{mg g}^{-1}$; $E/\text{kJ mol}^{-1}$.

That confirms the modelling of D-R for the adsorption system is acceptable. The calculated value of free sorption energy for the CFs1000°C and pFs ($E < 8 \text{ kJ mol}^{-1}$) presented in Table 1 indicates that physisorption played a significant role in the adsorption process at measured temperature range. For CFs400°C value of $E > 8 \text{ kJ mol}^{-1}$ suggests that adsorption can follow not only physisorption and a pore-filling mechanism but also through ion exchange. It can be explained by the presence of functional groups present on the surface that can react with drug molecules. The best adsorption properties of Dox exhibit CFs400°C. Obtained results stay in good agreement with pore distribution that indicate the CFs400 °C surface as the most potential for adsorption (mesopores). The rough surface of CFs1000°C exhibits a weak adsorption capacity. It can be explained by the presence of micropores the size of which does not correspond to the size needs of Dox as well as the marginal number of functional groups. The influence of temperature on Dox sorption on fibres is the most significant for temperature 323 K. Similar results were noticed in the case of paracetamol and ibuprofen on activated carbon^{47–49}. The explanation of the increase of efficiency of the adsorption process for higher temperatures can be explained by the solvation of drug molecules in an aqueous solution. The hydration shell is a barrier in the adsorption process and has to be removed. At higher temperatures, the thermic motions cause that the hydration sheaths are less stable, and the dehydration phenomenon occurs freely⁵⁰.

Thermodynamic functions as a standard change in Gibbs free energy ΔG° , the standard change in enthalpy ΔH° , and the standard change in entropy ΔS° form the basis of understanding the nature of the adsorption process. The thermodynamic equilibrium constant for the adsorption process K_0 allowed to determined ΔG° by using Eq. (8):

$$\Delta G^\circ = -RT \ln K_0 \quad (8)$$

where K_0 is equal to q_e/C_e and was determined from the intercept of $\ln(q_e/C_e)$ vs. q_e at temperature T (K), R is the universal gas constant.

The average standard enthalpy and entropy change for pFs and CFs400 °C were estimated from the slope and intercept of the linear form of the van 't Hoff equation:

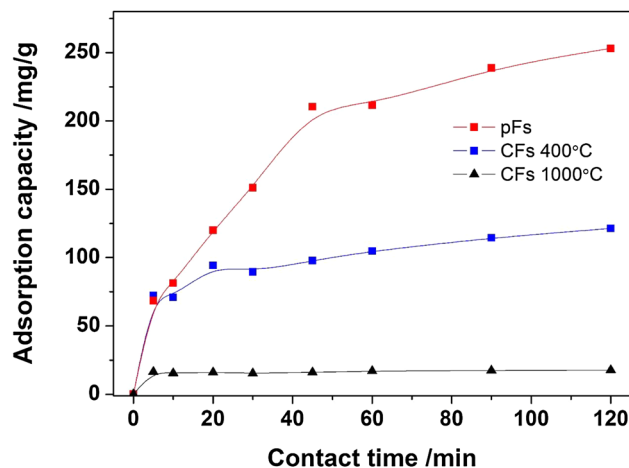


Figure 5. Influence of contact time on Dox adsorption capacity pF, CFs400 °C and CFs1000°C.

$$\ln K_0 = \frac{\Delta S^0}{R} - \frac{\Delta H^0}{RT} \quad (9)$$

Obtained parameters were presented in the supplementary materials in Table S5. Due to the poor adsorption performance of CFs1000°C in comparison to the CFs400°C, further studies on CFs1000°C were not carried out.

The adsorption process of Dox on the fibres is spontaneous; however, the amount of adsorbed drugs stays varied Table S5. It is worth noticing that the feasibility of adsorption as well as the experimental maximum adsorption capacity Q_{\max} is the highest for CFs400°C. Positive values of ΔS^0 suggest an irregular increase of randomness at the adsorbent/solution interface during the adsorption of the drug molecules on the carrier⁵¹. A similar tendency was observed in the case dyes adsorption on cation-exchange resin⁵² and Dox adsorption onto graphene oxide⁵³.

The value of the average standard change in enthalpy can be interpreted in terms of the type of adsorption. G. Bayramoglu and co-authors⁵² suggest that the value of ΔH^0 from the range between -20 to -40 kJ/mol reflects the physical adsorption whereas more negative values of ΔH^0 (range between -400 and -80 kJ/mol) reveals the prevalent contribution of chemisorption. Therefore, it can be said that obtained positive values of ΔH^0 confirm that the physical nature of the uptake dominates. The higher value of ΔH^0 obtained for CFs400°C reveals stronger interaction between Dox and CFs400°C than in case of pFs and as a result, leads to enhanced adsorption.

Kinetic studies of Dox adsorption and release. On the basis of the experimentally obtained adsorption kinetic curve in Fig. 5, it can be suggested that the adsorption process of Dox on CFs1000°C is very rapid and after 5 min reaches the almost maximal value of adsorption capacity equal ~ 17 mg g⁻¹. For CFs400°C and pFs the equilibrium is reached after 100 min; however, the adsorption process is more efficient compared to CF1000°C, which indicates the equilibrium adsorption capacity equal ~ 120 mg g⁻¹ and 250 mg g⁻¹ respectively Fig. 5.

Two kinetic models, which are pseudo-first-order (Lagergren, 1898) Eq. (10) and pseudo-second-order (Ho and McKay, 1999) Eq. (11) were applied to the experimental data^{53–55}.

$$\log \log (q_e - q_t) = \log q_e - \frac{k_1}{2.303} t \quad (10)$$

where: k_1 is the Lagergren rate constant of adsorption /min⁻¹, q_e and q_t denote the amounts of adsorption at equilibrium and at time t /mg g⁻¹, respectively.

$$\frac{t}{q_t} = \frac{1}{k_2 q_e^2} + \frac{t}{q_e} \quad (11)$$

where: k_2 is the pseudo second-order rate constant of adsorption /g mg⁻¹ min⁻¹, q_e and q_t denote the amounts of adsorption at equilibrium and at time t /mg g⁻¹, respectively.

The best fit and comparable values of experimental and calculated values of q_e were obtained for the pseudo second order kinetic model. Parameters of pseudo first and pseudo second kinetic models were presented in supplementary materials in Table S6.

Values of k_2 confirms that the adsorption rate changes in sequence: CFs1000°C > CFs400°C > pFs.

The kinetic results of the Dox release process are presented in Fig. 6. For CFs1000°C the percentage of release did not exceed 2% therefore the results were not presented.

Release of Dox accumulated on CF400°C does not exceed 6%. Low release of doxorubicin ($\sim 5\%$) was noticed for ion exchange microspheres at 298 K. However, temperatures of 316 K had up to 3 times higher release rates than 298 K⁵⁶. Drug release kinetics was used to determine the Dox release mechanism and best-fit drug release

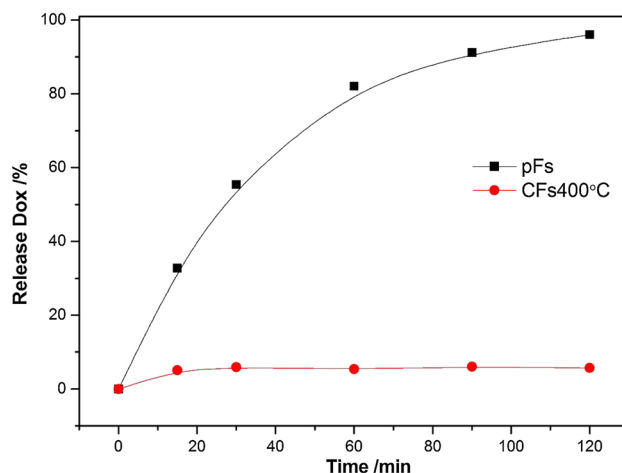


Figure 6. The release of Dox from pFs and CFs400°C at 298 K.

model. In this study, zero order, first order, second order, Higuchi, Weibull, and Korsmeyer–Peppas/Ritger–Peppas kinetic models were applied⁵⁷.

The zero-order kinetics model is expressed by the equation:

$$C_t = C_0 + K_0 t \quad (12)$$

where: C_t is the concentration of the drug released over time t , C_0 is the concentration of the drug in solution before release, and K_0 is the zero-order release rate constant.

The first-order kinetics model:

$$\ln(C_d - C_t) = \ln(C_d) - K_1 t \quad (13)$$

where C_t is the concentration of the drug released over time t , C_d is the concentration of the drug before dissolution and K_1 in the equation is the first-order release rate constant.

The second-order kinetics model represented by the equation:

$$\frac{1}{(C_d - C_t)} = \frac{1}{C_d} - K_2 t \quad (14)$$

where C_t is the concentration of the drug released over time t , C_d is the initial concentration of the drug and K_2 is the second-order rate constant.

Higuchi model considering a low concentration of the active agent in the matrix, where the solubility and release happen through the porosity of the matrix is expressed as:

$$C_t = K_H t^{\frac{1}{2}} \quad (15)$$

where C_t is the concentration of the drug released at time t and K_H is the Higuchi rate constant.

Weibull model represented by the equation:

$$C_m = C_s \left[1 - e^{-\frac{(t-T)^b}{a}} \right] \quad (16)$$

where C_m is the concentration of Dox dissolved as a function of time t , C_s is the total concentration of Dox being released, T means the latency time of the release process, a is the scale parameter which defines the timescale of the process and b characterizes the curves as either exponential ($b = 1$) S-shaped ($b > 1$) or parabolic ($b < 1$).

Korsmeyer–Peppas (Power Law) and Ritger–Peppas semi-empirical model:

$$C = \frac{C_t}{C_\infty} = K t^n \quad (17)$$

where C is the released concentration of the drug, C_t is the concentration of drug released over time t , C_∞ is the concentration of drug at the equilibrium state, K is kinetic constant (having units of t^n) incorporating structural and geometric characteristics of the delivery system, n is the diffusion exponent, which related to the drug release mechanism, in the function of time t .

The results of the application of different mathematical models to in-vitro drug release from pFs and CFs400°C were represented in Table 2.

Dox accumulated on CFs400°C and pFs display the first-order release. Many therapeutic systems display the first-order release for example betamethasone adsorbed on implants⁵⁸ or ibuprofen cumulated on carboxymethyl

Parameters			
CFs400°C		pFs	
The zero-order			
$K_0/\text{mg}^{-1} \text{min}^{-1}$	0.0097	$K_0/\text{g} \text{mg}^{-1} \text{min}^{-1}$	0.6571
r^2	0.8506	r^2	0.8717
The first-order			
K_1/min^{-1}	7.09×10^{-5}	K_1/min^{-1}	0.0269
r^2	0.9453	r^2	0.9985
The second-order			
$K_2/\text{ml} \text{g}^{-1} \text{min}^{-1}$	6.718×10^{-07}	$K_2/\text{ml} \text{g}^{-1} \text{min}^{-1}$	0.00169
r^2	0.905	r^2	0.8599
Higuchi			
$K_H/\text{mg} \text{ml}^{-1} \text{min}^{-1/2}$	0.1303	$K_H/\text{mg} \text{ml}^{-1} \text{min}^{-1/2}$	10.203
r^2	0.9559	r^2	0.9452
Weibull			
b	0.0617	b	1.013
r^2	0.9273	r^2	0.999
Power law			
K	0.04436	K	0.1154
n	0.0607	n	0.4504
r^2	0.905	r^2	0.958

Table 2. Parameters obtained from the kinetic models release of Dox from pFs and CFs400°C.

cellulose/mesoporous magnetic graphene oxide⁵⁹. The release mechanism of Dox from the polylactide spheres also followed the first-order⁶⁰.

The high degree of the correlation coefficient for the Higuchi kinetic model suggests that the prime mechanism of Dox release from the non-swellable matrix is diffusion controlled. Diffusion exponent $n \leq 0.5$ obtained from Power-law model also implies Fickian diffusion release Table 2.

The release of Dox from the functionalized mesoporous silica nanoparticles was also described by Thashini Moodley and Moganavelli Singh as undergoing rapid Fickian diffusion with no friction effects⁶¹.

In our opinion, the drug release process consists of two steps: the first rapid release called “burst of drug molecules” adsorbed at the surface (physisorbed by electrostatic and π - π dispersion interactions), and the second: drug release through pores. The release of covalently attached Dox depends on pH or temperature^{60,61}. The pH influence can be attributed to hydrogen bonding strength that decreases for the acidic environment and as result prompt the drug release. Thus, we expect that the release of covalently attached Dox in acidic pH (~ 5) occurs relatively fast. The weak drug release tendency for CFs400°C can be caused not only by the pore-blocking effect but mainly by hydrophobic hydration of carrier that hinders the water movement and consequently diffusion and drug release.

Conclusion

The findings of this study indicated that the best adsorption properties of Dox exhibit CFs400°C, although the specific surface area is very low ($\sim 13 \text{ m}^2 \text{ g}^{-1}$). It shows that molecules of Dox can locate only in pores which dimension higher than 4 nm. The increasing temperature induces the dehydration of the drug molecules that facilitate the adsorption that demonstrates visibly higher adsorption efficiency at 323 K for all investigated systems.

Adsorption of Dox is spontaneous for all fibres and positive values of ΔH° indicate that the physical nature of the uptake dominates. The main contribution of physisorption confirms also values of free sorption energy calculated based on the Dubinin-Radushkevich isotherm model. In case CFs400°C results obtained show that adsorption follows not only physisorption and a pore-filling mechanism but also through ion exchange. It can be explained by the presence of functional groups (phenolic mainly) determined by Boehm Titration and FT-IR spectra.

The kinetic models show that the prime mechanism of Dox release is diffusion controlled. The release of drugs from carbon fibres at 298 K is hindered. The reason for this fact can be the effect of pore-blocking as well as hydrophobic hydration of the fibres that obstruct the diffusion process.

In summary, obtained carbon fibres exhibit average adsorption and weak release of Dox. However, there are many possible ways of modifying their surface due to increase the drug adsorption and control the drug release. Thus, fibres can be considered as a material with significant potential for medical applications. What is more, a long time release is worth investigating.

References

- Sofla, R. L. M., Rezaei, M., Babaie, A. & Nasiri, M. Preparation of electroactive shape memory polyurethane/graphene nanocomposites and investigation of relationship between rheology, morphology and electrical properties. *Compos. B Eng.* **175**, 107090 (2019).
- Liu, Y., Dong, X. & Chen, P. Biological and chemical sensors based on graphene materials. *Chem. Soc. Rev.* **41**, 2283 (2012).
- Rauti, R., Musto, M., Bosi, S., Prato, M. & Ballerini, L. Properties and behavior of carbon nanomaterials when interfacing neuronal cells: How far have we come?. *Carbon* **143**, 430 (2019).
- Cataldo, F. Fullerenes. *Nanotubes Carbon Nanostruct* **10**, 293 (2002).
- Mostovoi, G. E., Kobets, L. P. & Frolov, V. I. Study of the thermal stability of the mechanical properties of carbon fibers. *Mech. Compos. Mater.* **15**, 20 (1979).
- Fedel, M. Hemocompatibility of carbon nanostructures. *J. Carbon Res.* **6**, 12 (2020).
- Yuan, X., Zhang, X., Sun, L., Wei, Y. & Wei, X. Cellular toxicity and immunological effects of carbon-based nanomaterials. *Part. Fibre Toxicol.* **16**, 18 (2019).
- Rahmati, M. & Mozafari, M. Biological response to carbon-family nanomaterials: Interactions at the nano-bio interface. *Front. Bioeng. Biotechnol.* **7**, 4 (2019).
- Baldrighi, M., Trusel, M., Tonini, R. & Giordani, S. Carbon nanomaterials interfacing with neurons: an in vivo perspective. *Front. Neurosci.* **10**, 250 (2016).
- Debnath, S. K. & Srivastava, R. Drug delivery with carbon-based nanomaterials as versatile nanocarriers: progress and prospects. *Front. Nanotechnol.* **3**, 644564 (2021).
- Zhang, Y. *et al.* Toxicity and efficacy of carbon nanotubes and graphene: the utility of carbon-based nanoparticles in nanomedicine. *Drug Metab. Rev.* **46**, 232 (2014).
- Shin, S. R. *et al.* Graphene-based materials for tissue engineering. *Adv. Drug Deliv Rev* **105**, 255 (2016).
- Sajid, M. I. *et al.* Carbon nanotubes from synthesis to *in vivo* biomedical applications. *Int. J. Pharm.* **501**, 278 (2016).
- Chen, M. *et al.* Nanodiamond-mediated delivery of water-insoluble therapeutics. *ACS Nano* **3**, 2016 (2009).
- Miao, P. *et al.* Recent advances in carbon nanodots: synthesis, properties and biomedical applications. *Nanoscale* **7**, 1586 (2015).
- Zhao, Q. *et al.* Mesoporous carbon nanomaterials in drug delivery and biomedical application. *Drug Delivery* **24**, 94 (2017).
- Ali-Boucetta, H. & Kostarelos, K. Pharmacology of carbon nanotubes: toxicokinetics, excretion and tissue accumulation. *Adv. Drug Deliv. Rev.* **65**, 2111 (2013).
- Balasubramanian, M. *Composite Materials and Processing* (CRC Press, Boca Raton, 2014).
- Saito, N. *et al.* Safe clinical use of carbon nanotubes as innovative biomaterials. *Chem. Soc. Rev* **40**, 3824 (2011).
- Petersen, R. Carbon fiber biocompatibility for implants. *Fibers Basel.* **4**, 1 (2016).
- Tarallo, L., Mugnai, R., Adani, R., Zambianchi, F. & Catani, F. A new volar plate made of carbon-fiber-reinforced polyetheretherketon for distal radius fracture: analysis of 40 cases. *J. Orthop. Traumatol.* **15**, 277 (2014).
- Bagheri, Z. S. *et al.* Biomechanical analysis of a new carbon fiber/flux/epoxy bone fracture plate shows less stress shielding compared to a standard clinical metal plate. *J Biomed Eng.* **136**, 091002 (2014).
- Clark, D., Nakamura, M., Miclau, T. & Marcucio, R. Effects of aging on fracture healing. *Curr. Osteoporos. Rep.* **15**, 601 (2017).
- Elias, K. L., Price, R. L. & Webster, T. J. Enhanced functions of osteoblasts on nanometer diameter carbon fibers. *Biomaterials* **23**, 3279 (2002).
- Samiezadeh, S., TavakkoliAvval, P., Fawaz, Z. & Bougherara, H. On optimization of a composite bone plate using the selective stress shielding approach. *J. Mech. Behav. Biomed. Mater* **42**, 138 (2015).
- Tan, Z. *et al.* Synthesis, structure, and properties of carbon/carbon composites artificial rib for chest wall reconstruction. *Sci. Reports* **11**, 11 (2021).
- Price, R. L., Waid, M. C., Haberstroha, K. M. & Webster, T. J. Selective bone cell adhesion on formulations containing carbon nanofibers. *Biomaterials* **24**, 1877 (2003).
- Czajkowska, B. & Blazewicz, M. Phagocytosis of chemically modified carbon materials. *Biomaterials* **18**, 69 (1997).
- Bai, Y., Keller, T. & Vallée, T. Modeling of stiffness of FRP composites under elevated and high temperatures. *Compos. Sci. Technol.* **68**, 3099 (2008).
- Okayasu, M. & Tsuchiya, Y. Mechanical and fatigue properties of long carbon fiber reinforced plastics at low temperature. *J. Sci. Adv. Mater. Devices* **4**, 577 (2019).
- Chudoba, D., Ludzik, K., Jazdzewska, M. & Woloszczuk, S. Kinetic and equilibrium studies of doxorubicin adsorption onto carbon nanotubes. *Int. J. Mol. Sci.* **21**, 8230 (2020).
- Sanson, C. *et al.* A simple method to achieve high doxorubicin loading in biodegradable polymersomes. *J Control Release* **147**, 428 (2010).
- Ayawei, N., Ebelegi, A.N., & Wankasi, D., Modelling and interpretation of adsorption isotherms. *Hindawi J. Chem.* 3039817 (2017)
- Azizian, S. Kinetic models of sorption: a theoretical analysis. *J. Colloid Interface Sci.* **276**, 47 (2004).
- Hamdaoui, O. & Emmanuel, N. Modeling of adsorption isotherms of phenol and chlorophenols onto granular activated carbon. Part I. Two-parameter models and equations allowing determination of thermodynamic parameters. *J. Hazardous Mater.* **147**, 381 (2007).
- Langmuir, I. The constitution and fundamental properties of solids and liquids Part I Solids. *J. Am. Chem. Soc.* **38**, 2221 (1916).
- Freundlich, H. M. F. Over the adsorption in solution. *Z. Phys. Chem.* **57**, 385 (1906).
- Dubinin, M. M. & Radushkevich, L. V. The equation of the characteristic curve of activated charcoal. *Proc. Acad. Sci. USSR Phys. Chem. Sect.* **55**, 331 (1947).
- Kayal, S. & Ramanujan, R. V. Doxorubicin loaded PVA coated iron oxide nanoparticles for targeted drug delivery. *Mater. Sci. Eng. C* **30**, 484 (2010).
- Depan, D., Shah, J. & Misra, R. D. K. Controlled release of drug from folate-decorated and graphene mediated drug delivery system: Synthesis, loading efficiency, and drug release response. *Mater. Sci. Eng. C* **31**, 1305 (2011).
- Kumar, P. S. *et al.* Adsorption equilibrium, thermodynamics, kinetics, mechanism and process design of Zinc(II) ions onto cashew nut shell. *Can. J. Chem. Eng.* **90**, 973 (2012).
- Kundu, S. & Gupta, A. K. Arsenic adsorption onto iron oxide-coated cement (IOCC): regression analysis of equilibrium data with several isotherm models and their optimization. *Chem. Eng. J.* **122**, 93 (2006).
- Onyango, M. S., Kojima, Y., Aoyi, O., Bernardo, E. C. & Matsuda, H. Adsorption equilibrium modeling and solution chemistry dependence of fluoride removal from water by trivalent-cation-exchanged zeolite F-9. *J Colloid Interf. Sci.* **279**, 341 (2004).
- Helfferich, F. *Ion Exchange* (McGraw-Hill Book Co., 1962).
- Chen, H., Zhao, J., Dai, G., Wu, J. & Yan, H. Adsorption characteristics of Pb(II) from aqueous solution onto a natural biosorbent, fallen cinnamomum camphora leaves. *Desalination* **262**, 174 (2010).
- Tahir, S. S. & Rauf, N. Removal of a cationic dye from aqueous solutions by adsorption onto bentonite clay. *Chemosphere* **63**, 1842–1848 (2006).

47. Mestre, A. S., Pires, J., Nogueira, J. M. F. & Carvalho, A. P. Activated carbons for the adsorption of ibuprofen. *Carbon* **45**, 1979 (2007).
48. Villaescusa, N. F., Poch, J., Bianchi, A. & Bazzicalupi, C. Mechanism of paracetamol removal by vegetable wastes: The contribution of π - π interactions, hydrogen bonding and hydrophobic effect. *Desalination* **270**, 135 (2011).
49. Baccar, R., Sarràb, M., Bouzida, J., Fekic, M. & Blázquez, P. Removal of pharmaceutical compounds by activated carbon prepared from agricultural by-product. *Chem. Eng. J.* **211–212**, 310 (2012).
50. Naseem, R. & Tahir, S. S. Removal of Pb(II) from aqueous/acidic solutions by using bentonite as an adsorbent. *Water Res.* **35**, 3982 (2001).
51. Jedynak, K., Wideł, D. & Rędzia, N. Removal of rhodamine B (a basic dye) and acid yellow 17 (an acidic dye) from aqueous solutions by ordered mesoporous carbon and commercial activated carbon. *Colloids Interfaces* **3**, 30 (2019).
52. Bayramoglu, G., Altintas, B. & Arica, M. Y. Adsorption kinetics and thermodynamic parameters of cationic dyes from aqueous solutions by using a new strong cation-exchange resin. *Chem. Eng. J.* **152**, 339 (2009).
53. Wu, S. *et al.* Adsorption properties of Doxorubicin hydrochloride onto graphene oxide: equilibrium, kinetic and thermodynamic studies. *Materials* **6**, 2026 (2013).
54. Hubbe, M. A., Azizian, S. & Douven, S. Implications of apparent pseudo-second-order adsorption kinetics onto cellulosic materials: A review. *BioRes* **14**, 7582–7626 (2019).
55. Chen, X. Modeling of experimental adsorption isotherm data. *Information* **6**, 14 (2015).
56. Burton, M. A. *et al.* In vitro and in vivo responses of doxorubicin ion exchange microspheres to hyperthermia. *Int. J. Hyperthermia* **8**, 485 (1992).
57. Mircioiu, C. *et al.* Mathematical modeling of release kinetics from supramolecular drug delivery systems. *Pharmaceutics* **11**, 140 (2019).
58. Wójcik-Pastuszka, D., Krzak, J., Berkowski, R., Osiński, B. & Musiał, W. Evaluation of the release kinetics of a pharmacologically active substance from model intra-articular implants replacing the cruciate ligaments of the knee. *Mater. Basel* **12**, 1202 (2019).
59. Farazi, R., Vaezia, M. R., Molaei, M. J., Saeidifar, M. & Behnam-Ghaderi, A. A. Effect of pH and temperature on doxorubicin hydrochloride release from magnetite/graphene oxide nanocomposites. *Mater. Today: Proc.* **5**, 15726 (2018).
60. Mhlanga, N. & Ray, S. S. Kinetic models for the release of the anticancer drug doxorubicin from biodegradable polylactide/metal oxide-based hybrids. *Int. J. Biol. Macromol.* **72**, 1301 (2015).
61. Moodley, T. & Singh, M. Sterically stabilised polymeric mesoporous silica nanoparticles improve doxorubicin efficiency: Tailored cancer therapy. *Molecules* **25**, 742 (2020).

Acknowledgements

This work was supported by the grant from the Polish Plenipotentiary in Joint Institute for Nuclear Research, Dubna, Russia (Regulation no 104 of 22.02.2019, article 8).

Author contributions

D.C. designed the whole work, coordinated the study, wrote and revised the manuscript. K.Ł. interpreted data and participated in writing the manuscript. M.J. interpreted data and revised the manuscript. All authors have read and agreed to the published version of the manuscript.

Funding

The funders had no role in the design of the study; in the collection, analyses, or interpretation of data; in the writing of the manuscript, or in the decision to publish the results.

Competing interests

The authors declare no competing interests.

Additional information

Supplementary Information The online version contains supplementary material available at <https://doi.org/10.1038/s41598-022-06044-7>.

Correspondence and requests for materials should be addressed to D.C.

Reprints and permissions information is available at www.nature.com/reprints.

Publisher's note Springer Nature remains neutral with regard to jurisdictional claims in published maps and institutional affiliations.



Open Access This article is licensed under a Creative Commons Attribution 4.0 International License, which permits use, sharing, adaptation, distribution and reproduction in any medium or format, as long as you give appropriate credit to the original author(s) and the source, provide a link to the Creative Commons licence, and indicate if changes were made. The images or other third party material in this article are included in the article's Creative Commons licence, unless indicated otherwise in a credit line to the material. If material is not included in the article's Creative Commons licence and your intended use is not permitted by statutory regulation or exceeds the permitted use, you will need to obtain permission directly from the copyright holder. To view a copy of this licence, visit <http://creativecommons.org/licenses/by/4.0/>.

© The Author(s) 2022